

Z-SCHEME PHOTOCATALYTIC DEGRADATION OF REACTIVE ORANGE 16 (RO16) DYE OVER TUNGSTEN TRIOXIDE AND CADMIUM SULFIDE (WO₃-CdS) COMPOSITE UNDER VISIBLE LIGHT IRRADIATION

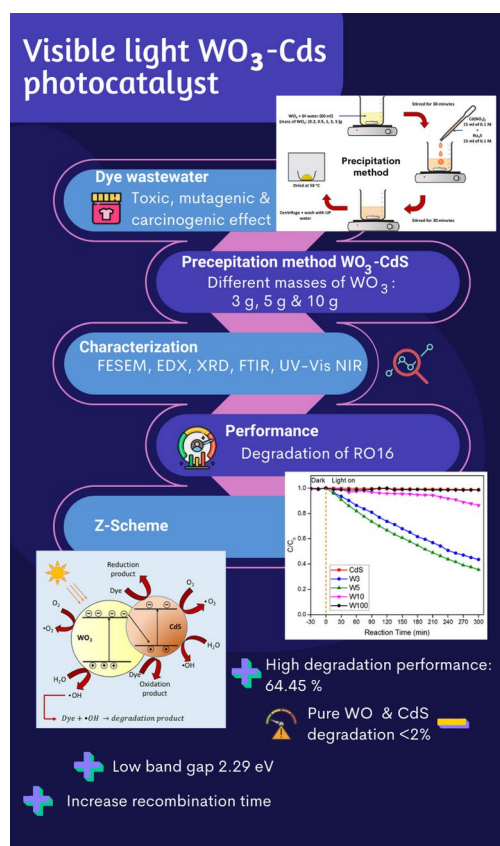
Mohd Izzat Iqbal Mohd Zahar, Roziana Kamaludin, Mohd Hafiz Dzarfan Othman*, Mohd Hafiz Puteh, Mukhlis A Rahman, Juhana Jaafar

Advanced Membrane Technology Research Centre (AMTEC), Universiti Teknologi Malaysia, 81310 UTM Johor Bahru, Johor, Malaysia

Article history
Received
08 October 2023
Received in revised form
03 January 2024
Accepted
07 January 2024
Published online
30 November 2024

*Corresponding author
hafiz@petroleum.utm.my

Graphical abstract



Abstract

The escalating global concern over dye wastewater pollution, characterized by its harmful effects, has sparked interest in visible light-activated photocatalysis for cost-effective industrial wastewater treatment. The study focused on visible light-activated photocatalysts, notably cadmium sulfide (CdS) with a 2.4 eV band gap energy and tungsten trioxide (WO₃) known for its resilience to photo degradation, durability across various pH conditions, and a 2.7 eV band gap energy. However, CdS is susceptible to photo anodic corrosion, while WO₃ exhibits low photocatalytic degradation performance due to rapid recombination between excited electrons and electron holes from low-energy visible light. The Z-scheme electrons transfer photocatalyst (WO₃-CdS) was designed to extend recombination time and maintain WO₃ stability. This visible light-activated composite was synthesized through a simple and cost-effective precipitation method. CdS were kept constant while mass of WO₃ were varied for 3 g, 5 g, 10 g. Structural and morphological analyses were conducted using various techniques, including field emission scanning electron microscopy (FE-SEM), energy dispersion of X-ray (EDX), Fourier transform infrared (FTIR), X-ray diffraction (XRD), and UV-Vis-NIR spectrophotometer to analyze various properties. The synthesized composite of WO₃-CdS successfully lowered the band gap energy to 2.28 eV and shifted the photon absorption more towards the visible spectrum. When applied to the photo degradation of reactive orange 16 (RO16) under visible light for 300 minutes, the WO₃-CdS composite exhibited a remarkable 64.45 % degradation rate, surpassing pure CdS and WO₃ rates of only around 1.18 % each. The Z-scheme electron transfer process between CdS and WO₃ significantly enhanced catalytic efficiency. This achievement holds promise for sustainable wastewater remediation, marking a notable advancement in the field.

Keywords: Photocatalysis, Energy storage, WO₃, CdS, Visible light driven

© 2024 Penerbit UTM Press. All rights reserved

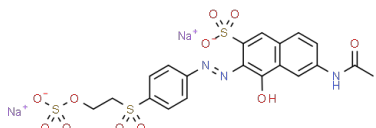
1.0 INTRODUCTION

At the outset of 1856, the world of dye industries experienced a momentous transformation that would forever alter the landscape of color. It was in this era that WH Perkin's remarkable discovery of mauve opened the door to the

production of modern synthetic dyes [1]. Over the course of the following century, this breakthrough would lead to the synthesis of an astonishing array of hues, with millions of distinct colored compounds coming into existence. Among these, an astounding 15,000 colorants would go on to be produced at an industrial scale, coloring our world in ways previously unimaginable [2].

Owing to high degree of photolysis and chemical stability, along with their high ability to bind with textile fibers via the covalent bonds, reactive orange (RO16) dye (Colour Index Number: 17757, Molecular Formula: $C_{20}H_{17}N_3O_{11}S_3Na$, Molecular weight: 617.53 g/mol) is extensively used as colorant. The chemical structure and its absorption maxima (λ_{max}) are given in Table 1. This characteristic ensure long lasting colour being preserved and making it hard to be removed from washing process as strong adhesion between reactive dye and fiber is formed [3].

Table 1 Chemical structure and absorbance maxima of dye

Name	Chemical Structure	λ_{max} (nm)
Reactive Orange 16		494 [4]

Even though reactive dyes have good interaction with the fabric, it wastewater poses numerous undesirable impacts on environment and human being. The wastewater from dyeing stage usually presents as toxic, mutagenic and carcinogenic effect on aquatic life [5].

To overcome the ever increasing dye wastewater problem, an extensive range of wastewater treatment has been studied. Current treatments include coagulation flocculation sedimentation, adsorption, biological, electrochemical, membrane separation or filtration and chemical oxidation [6]. Photocatalytic dye degradation is considered as an attractive and versatile method due to low cost material, biodegradable, reusable, low energy consumption and most importantly highly effective. The widespread utilization of photocatalytic methods for eliminating diverse organic and inorganic dyes from contaminated water has prompted researchers to enhance their explorations into the feasibility of photocatalytic technology as an effective solution for dye elimination in wastewater treatment.

However, most of earlier study revolves around metal oxide such as titanium oxide, chromium oxide and zinc oxide [7]. These metal oxides are ultraviolet (UV) activated light which only cover around 5 % of our solar spectrum that reach surface of the earth [8]. This makes the photocatalytic activity is not fully utilized, instead lots of solar energy being wasted. Moreover, UV light has been proved to be hazardous to human and other living organisms. It has been reported that UV is directly associates with both melanoma and non-melanoma skin cancer, as well as a variety of other dermatological conditions and mutation to expose skin [9].

The solution to this challenge becomes clear when we set our sights on the intriguing task of reducing the band gap of photocatalysts, making them more receptive to the visible light territory. To achieve this objective, several methods have been used, for instance by using narrow band gap energy photocatalysts. Alternatively, modification of photocatalysts with non-metal doping, metal deposition, composite photocatalysts, defect induced visible light active (VLA) photocatalysis, dye sensitization in photocatalysis and oxygen rich TiO_2 modification are considered feasible to narrower the band gap energy [10].

Some of narrow band gap materials are cadmium sulfide (CdS), iron (III) oxide (Fe_2O_3), and bismuth based material such as bismuth vanadate (BiO_4V) [10]. CdS, with its band gap measuring 2.4 electronvolts (eV), corresponds to a wavelength of approximately 516.6 nm in the electromagnetic spectrum. This specific band gap places CdS in a favourable position for absorbing visible light efficiently. In practical terms, this means that when CdS is exposed to visible light, it readily captures and utilizes the energy from this light, which is vital for various photocatalytic processes.

The inherent characteristic of CdS renders it a highly favorable option for harnessing its photocatalytic potential, particularly when it comes to being activated by visible light. The presence of visible light, which constitutes a significant portion of both natural sunlight and artificial lighting, endows CdS with versatility, rendering it suitable for a diverse array of applications. These applications encompass environmental remediation, water purification, and the conversion of solar energy.

Nevertheless, it's important to note that CdS does have a significant drawback, particularly in aqueous environments. When exposed to water and light, CdS can be vulnerable to a phenomenon known as photoanodic corrosion. In this process, the CdS material can undergo degradation due to the simultaneous presence of water and light. This degradation may lead to the discharge of toxic cadmium ions into the nearby surroundings, posing environmental and health concern [10].

To tackle the challenge of photoanodic corrosion and enhance the overall performance of CdS photocatalysts, researchers frequently adopt a strategy that involves integrating CdS with other types of photocatalysts. Two commonly used co-catalysts for this purpose are titanium dioxide (TiO_2) and zinc oxide (ZnO) [11]. This composite combination able to enhance the durability of photocatalysts and expand photocatalytic performance. Presently, there is a growing focus on studying composite combinations that enhance performance by collectively increasing various factors, including crystallinity, charge carrier mobility, porosity, active facets, and surface area [12].

Tungsten trioxide (WO_3), sometimes known as tungsten (VI) oxide, is a material characterized by its narrow band gap which is 2.7 eV, that equivalent to a wavelength of 459.2 nm. WO_3 demonstrates its capacity to serve as a photocatalyst when stimulated by visible light. WO_3 has showcased remarkable effectiveness in breaking down organic substances. This narrow band gap enables WO_3 to harvest almost 30 % of sunlight which is stark different compare to TiO_2 that only utilize 5 % of the sunlight [13]. Additionally, WO_3 exhibits a range of fascinating properties, including high photosensitivity, resistance to photo degradation, non-toxicity, and robust stability in various conditions, even in environments with a pH below 8 and acidic conditions. These distinctive properties position it as a highly desirable option for a wide array of wastewater treatment applications. It shines particularly in the elimination of challenging substances, for instance, fabric dyes, microbial agents, and specific organic substances. In the realm of textile wastewater treatment, WO_3 exceptional photocatalytic prowess comes to the forefront, efficiently breaking down complex dye molecules and rendering the water clear and safe. Furthermore, its bactericidal properties make it a valuable tool for disinfecting water contaminated with harmful

microorganisms. Beyond that, it exhibits remarkable efficiency in degrading various organic contaminants, contributing significantly to the purification of water resources. In essence, the versatility and effectiveness of WO_3 make it a robust and sustainable solution for addressing the diverse and pressing challenges of wastewater treatment [14].

The process of synthesizing composites to create heterostructures, has demonstrated to be a highly effective approach for boosting the performance of photocatalysis. Some examples of composite photocatalysts include ZnO-TiO_2 , CdS-TiO_2 , and $\text{Bi}_2\text{S}_3\text{-TiO}_2$. These combinations leverage the unique properties of different materials to improve their overall photocatalytic efficiency [10]. One of the main factor that contributes to increase in the recombination time of composite photocatalyst is due to Z-scheme formation between the two catalysts [11]. A significant number of photocatalysts that are activated by visible light owe their remarkable efficiency to possessing a low band gap energy. This is a crucial attribute as it dictates the quantity of energy needed to stimulate electrons (e^-) from the valence band to the conduction band within the photocatalyst material. This energy transition simultaneously generates a vacant space known as a hole (h^+) in the valence band.

Advantages of having a low band gap energy becomes evident for photocatalysis where it means that relatively low-energy photons from the visible light spectrum can be employed to trigger this electron transition. In other words, visible light, which encompasses a considerable percentage of the sunlight spectrum, carries enough energy to promote electrons from the valence band to the conduction band. Concurrently, this progression produce a hole in the valence band [15].

Hence, these photocatalysts were able to utilize full spectrum of visible light irradiation. However, this attribute come at a cost, low band gap energy means the excited electrons have smaller kinetic energy. This will result in quick recombination between excited electrons and hole, making it hard for it to be consume in oxidation or reduction process with the pollutant [16]. As a result, most of visible light photocatalysts has minimal efficiency of pollutant degradation [17].

Several studies have demonstrated that composite photocatalysts can considerably improve photocatalytic effectiveness by extending the recombination time of photocatalyst electron and hole pairs compared to conventional photocatalyst structures. An example of this improvement can be perceived in the event of CuS-WO_3 composite photocatalysts [18]. These composites structure has the ability to further reduce a wide band gap towards visible light active photocatalysts such as composite of $\text{TiO}_2\text{-CdS}$ [19]. Additionally, they compensate each other shortcomings as individual photocatalysts and induce collective effect such as an improvement of photo stability and efficient charge separation as can be seen on ZnO-CdS composite [11].

In this investigation, CdS was chosen as the foundational material for the CdS-WO_3 composite due to its possessing a low band gap energy. The incorporation of WO_3 was intended to facilitate the establishment of a Z-scheme configuration between the two photocatalysts. This composite structure effectively extended the duration during which electrons and holes recombined, resulting in a boost to photocatalytic effectiveness whilst exposed to visible light. Furthermore, the

introduction of WO_3 addressed a notable drawback of CdS photocatalysts, namely their susceptibility to photo degradation in aqueous solutions, thereby bolstering their stability. The preparation of pure CdS and $\text{WO}_3\text{-CdS}$ composite involved a one-step precipitation method, and various spectroscopic and analytical techniques were employed to scrutinize pure CdS , WO_3 , and the $\text{WO}_3\text{-CdS}$ composite. In addition, the photocatalytic prowess of each photocatalyst was meticulously assessed in the context of its ability to degrade RO16 dye when exposed to visible light. It is worth highlighting that this study has introduced a groundbreaking Z-scheme photocatalytic mechanism, showcasing the remarkable improvement of photocatalytic effectiveness in the degradation of RO16 through the synergistic interaction between WO_3 and CdS .

2.0 METHODOLOGY

2.1 Materials

All the chemicals utilized in the production of the composite photocatalyst for visible light were procured from Sigma-Aldrich, USA, and were employed without any additional cleansing. We employed deionized (DI) water and ultra-pure (UP) water throughout our experiments. The materials used, including cadmium nitrate ($\text{Cd}(\text{NO}_3)_2$) (with a purity of 98.0 %) and tungsten (VI) oxide (WO_3) (with a particle size below 100 nm), were of analytical reagent grade. Additionally, sodium sulfide hydrate (Na_2S) (with a purity of 60 %) was employed in the synthesis process.

2.2 Synthesis of Visible Light Photocatalysts: Tungsten (VI) Oxide – Cadmium Sulfide ($\text{WO}_3\text{-CdS}$) Composite

Synthesis of visible light photocatalysts with optimum RO16 degradation was conducted using tailored Jin's single step precipitation method [20]. To begin, different quantities of WO_3 nanopowder particles were evenly distributed in deionized (DI) water with a volume of 60 ml and agitated for a period of 10 minutes using a magnetic stirring apparatus. The various masses of WO_3 which were 3 g, 5 g, and 10 g were labelled with W3, W5 and W10 respectively, while pure WO_3 , was labelled as W100. Furthermore, pure CdS was synthesized without WO_3 and labelled as CdS . In contrast, volume used to precipitate CdS were kept constant and the weight percentages of the composite photocatalyst calculated from theoretical stoichiometry is shown in Table 2. The selection of specific amounts of WO_3 was strategically determined to analyze the impact of its concentration on the performance of $\text{WO}_3\text{-CdS}$ photocatalyst. Lower and higher amounts, 3 g and 10 g respectively, were chosen to represent the extremes of the concentration range, while the intermediate amount of 5 g provides a midpoint for comparative purpose. This deliberate variation aims to capture potential concentration-dependent effects on photocatalytic activity, ensuring thorough examination of the material's behaviour across different loading levels.

Table 2 Shows comparison between weight percentages of WO_3 and CdS calculated from theoretical stoichiometry and atomic percentages obtained from EDX analysis

Sample Name	Weight %		Atomic %			
	WO ₃	CdS	W	O	Cd	S
CdS	0	100.0	0	0	85.2	14.8
W3	34.1	65.9	11.3	15.7	56.6	16.4
W5	46.3	53.7	33.8	24.8	31.5	9.9
W10	96.4	3.6	50.7	25.8	19.4	4.1
W100	100.0	0	68.0	32.0	0	0

Afterwards, 25 ml of both Cd(NO₃)₂ and Na₂S was prepared in separate beaker. Both of this solution have 0.1 mol of solute in one litre solution. The Cd(NO₃)₂ the solution was carefully dispersed in a gradual manner, with stirring, to the previously dispersed WO₃. This solution was then continuously stirred for 30 minutes at room temperature. Afterward, Na₂S was added using the same method employed for Cd(NO₃)₂. Following the precipitation process, all samples underwent centrifugation and were subsequently rinsed with UP water five times before undergoing another round of centrifugation. Then, the samples were exposed to a 24-hour drying period in a vacuum oven at temperature of 50 °C and stored in Schott bottles fully wrapped in aluminum foil to protect them from any light source. Figure 1 illustrates the precipitation method employed in this process.

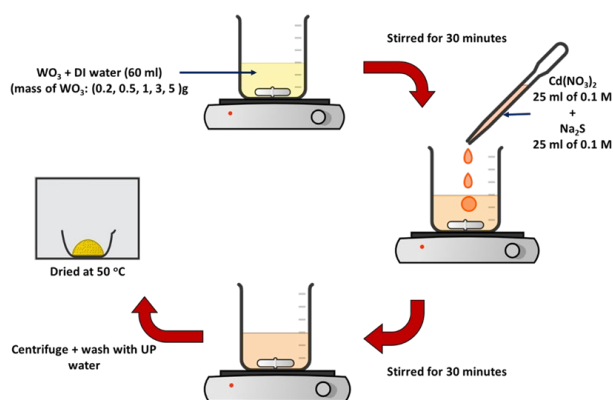


Figure 1 Preprecipitation method of WO₃-CdS composite preparations

2.3 Characterization of WO₃-CdS Photocatalysts

The analysis involved the investigation of surface characteristics. Qualitative assessments of the prepared WO₃-CdS photocatalysts were conducted using a field emission scanning electron microscope (FE-SEM; Model: SU2080, Hitachi) at an accelerated voltage of 2000 V. To assess the existence and distribution of elements, including W, O, Cd, and S in the WO₃-CdS photocatalysts within the composite powders, energy dispersion X-ray line scan spectrum (EDX; Model: X-MaxN 51-XXM1011, Oxford Instrument) was employed. This method assesses the proportional occurrence of released X-rays in relation to their energy levels.

For chemical structure analysis, varying weight percentages of WO₃-CdS photocatalysts undergo scrutiny through Fourier Transform Infrared (FTIR) spectroscopy using a Perkin Elmer FT-IR instrument. These photocatalysts were subjected to an infrared beam spanning wavelengths from 650 cm⁻¹ to 4,000 cm⁻¹. The resulting FTIR spectra provided absorbance

data, revealing peaks at specific frequencies that corresponded to the vibrational modes of chemical bonds within the samples. To confirm the chemical database and subsequently have better understanding on photocatalyst structure and composition, the collected FTIR data was compared with spectral databased. The positions and intensities of these peaks, the types of chemical bonds present, including those from WO₃ and CdS were analyzed and identified.

Shifting to crystallinity analysis, an advanced X-Ray Diffractometer (SIEMENS D5000 model) conducts comprehensive X-ray Diffraction (XRD) analysis. Operating at 40,000 V and 40 mA with copper K-α radiation, this examination covers an angular range of 2θ from 20° to 80°, providing insights into the complex arrangement and phase formation of the WO₃-CdS composite.

Concluding with optical property analysis, a Ultra-Violet, Visible, and Near Infra-Red (UV-Vis-NIR) spectrophotometer (UV-3101PC model, manufactured by Shimadzu) analyzes wavelengths from 200 nm to 800 nm. The KBr approach was employed for accurate spectral measurements, this investigation offers in-depth understanding of the photocatalysts optical attributes and absorption spectrum across the UV-Vis-NIR range.

2.4 Performance of Visible Light Activated Photocatalysts on RO16 Dye

During the initial phase of photocatalysis with a RO16 solution, the prepared WO₃-CdS photocatalysts are expected to undergo an adsorption-desorption process. To determine the concentration and the time required for this process to reach equilibrium, 0.25 g of the prepared WO₃-CdS photocatalyst was mixed with 250 ml of RO16 with a content of 10 milligrams per liter (mg/L). The solution was stirred in the dark until it reached adsorption-desorption equilibrium.

To confirm equilibrium, 10 ml samples of the suspension were taken every 15 minutes and filtered through a 0.45 μm polyamide syringe filter to subtract any surplus photocatalyst prior to evaluation. Afterwards, variation in absorbance of the exposed RO16 sample over time in the experiment was assessed employing a UV-Vis Spectrometer (HACH, DR5000) at 494 nm and was contrasted with a control sample (RO16 solution in the absence of photocatalyst). This process was repeated until the concentration of RO16 became stable and this stable point is considered as the initial concentration (C₀).

The photocatalytic efficiency of the produced WO₃-CdS composites was assessed using an RO16 dye suspension under visible light irradiation. A commercial high-purity WO₃ sample was employed as a control experiment, used as purchased, with no further purification. Subsequently, the suspension was exposed to visible light from a 100 Watt White LED floodlight while being stirred. The high intensity of the visible light source was chosen to maximize the efficiency of the photocatalytic process. An air diffuser was used to ensure an adequate supply of oxygen (O₂) for the reaction. The experimental setup is depicted in Figure 2. Using the previously described collection method, suspensions were gathered at regular time intervals (C_t).

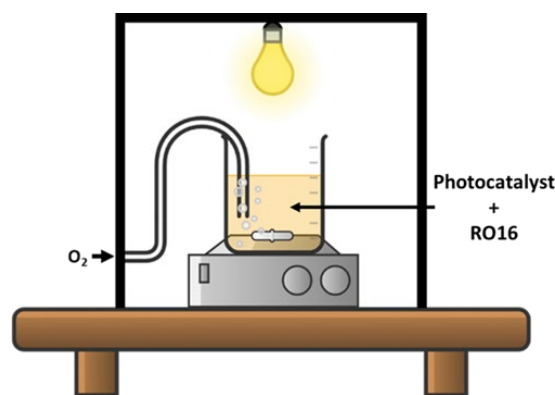


Figure 2 Experimental setup during measurement of photocatalytic activity on RO16 by WO_3 -CdS photocatalysis under visible light

The optical assessment of all photocatalyst samples, both prior to and following irradiation was employed to determine the degradation efficiency of RO16, which is expressed through the following equation:

$$DRO16 = \frac{C_o - C_t}{C_o} \times 100$$

In this equation, DR016% represents the percentage degradation of RO16, C_o is the commencing concentration when time is $t = 0$, just before the suspension is irradiated with visible light, C_t is the concentration time t is at 15, 30, 45, 60, 75, 90, 105, 135, 165, 195, 225, 255, 285 and 300 minutes after irradiation. Both C_t and C_o in Equations 1 and 2 are in mol/L. These values will be determined using Beer – Lambert Law from absorbance values obtained using UV-Vis spectroscopy. Additionally, the rate of WO_3 -CdS degradation reaction (k) at a particular point in time will be measured employing the subsequent formula:

$$\ln \frac{C_o}{C_t} = kt$$

3.0 RESULTS AND DISCUSSION

3.1 Morphologies of (WO_3 -CdS) Composite Photocatalyst

Comprehensive exploration for morphological characteristics of the prepared CdS, WO_3 , and WO_3 -CdS composites, each with varying weight percentages, was carried out employing FE-SEM, and the resulting micrographs are thoughtfully depicted in Figure 3 (a-e). This microscopic analysis unveiled intriguing insights into the surface features and particle distributions of these materials. Notably, the micrographs (Figure 3a and 3e) vividly portray the distinct surface topographies of CdS and WO_3 particles. CdS particles exhibited a notable tendency towards rounded edges, a characteristic that was distinctly different from the WO_3 particles, which exhibited sharper and more defined edges.

The most intriguing aspect, however, emerges when focusing on the composite WO_3 -CdS photocatalysts with varying weight

percentages, denoted as W3, W5, and W10. As revealed in the particle size distribution graph (Figure 3b, 3c, and 3d), both CdS and WO_3 particles coexist, showing non-uniform sizes that contribute to the composite's heterogeneity. This unique blend of particles with different sizes and properties is crucial in manipulating the photocatalytic behaviour and material functionality.

Moreover, to quantify the average particle size for each of these composite samples, a meticulous approach was taken. The estimation method employed, known as Paswan's method, involves matching the histogram of particle size distribution to a log-normal distribution [21]. The function is expressed as follows:

$$f(D) = \left(\frac{1}{\sqrt{2\pi}\sigma_D} \right) e^{-\left[\frac{\ln^2(D/D_o)}{2\sigma^2} \right]}$$

In the context of our analysis, D represents the average particle size, and σ_D denotes the standard deviation. The outcomes of this particle size examination have been meticulously visualized in Figure 4, providing a graphical representation of the estimated average particle sizes based on a sample size of 100 particles. This thorough analysis has yielded intriguing insights into how variations in material composition have impacted particle size.

While focusing on WO_3 particles size change, a distinct trend becomes evident. When the weight percentages of WO_3 , transitioning from sample W3 to W5 and W10 increases, there is an evident reduction in the average particle size. In contrast, pure WO_3 , designated as W100, exhibits the smallest average particle size among all the samples, measuring at 100 nm. The probable explanation for this reduction in particle average size is due to increase in mass of WO_3 . This will lead to a higher solvent concentration and will intensify the solvent viscosity. As a result, diffusion of solvent molecules becomes more challenging due to reduce molecular mobility and subsequently increased in precipitation time. This, in turn, will result in decrease of particle size [22].

On the other hand, the analysis of CdS particles exposes a contrasting pattern. As the WO_3 load increases, generally, the average size of CdS particles would generally increase, as can be observed in samples CdS, W3, and W5, with mean dimensions of 11 nm, 25 nm, and 31 nm respectively. However, the W10 sample deviates from this trend, where it obtained an average CdS particle size of 11 nm. This unique observation might be due to complex interactions between the two materials within the composite, which could have influenced the growth of CdS particles differently [23, 24].

Furthermore, in the framework of particle growth, several factors come into play. When WO_3 particles were hosted into the composite at higher concentrations, it may lead to increased interactions at the molecular level. This has potential to affect the nucleation and growth of CdS particles. The presence of WO_3 could serve as nucleation sites for CdS particles to form, potentially resulting in smaller CdS particles. Alternative explanation for this phenome is the solubility of CdS in the solvent might impacting its precipitation behaviour and leading to smaller particle sizes. Besides that, the intricate interplay of forces, for instance, electrostatic forces, Van der Waals forces, and steric effects between the two constituents,

can influence their aggregation and growth. These interactions can vary depending on the concentration of WO_3 and the overall composition of the composite, leading to variations in CdS particle size.

Overall, this detailed analysis of particle sizes elucidated the intricate relationship between material composition and particle size variations. It underscored the importance of solvent characteristics and mass concentration in shaping particle sizes.

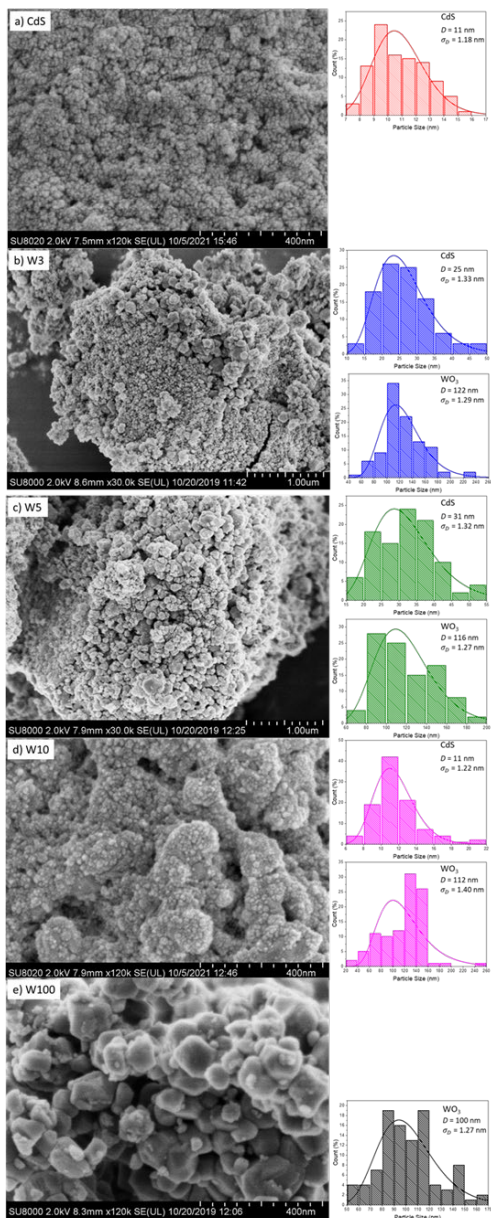


Figure 3 FE-SEM images of WO_3 -CdS were captured at various loadings of: a) CdS, b) W3, c) W5, d) W10 and e) W100. Each image includes an inset showing the particle size distribution, which has been matched with a log-normal distribution function for each respective sample.

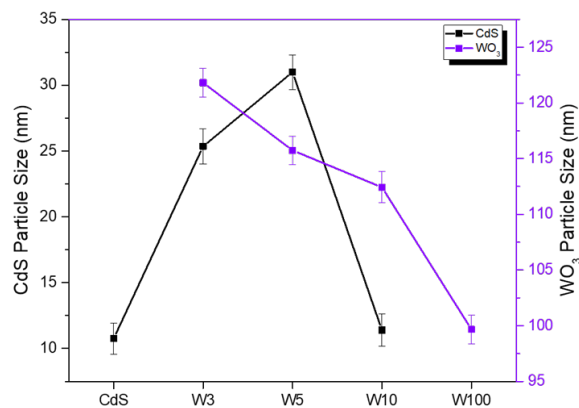


Figure 4 Mean particle size dispersion of CdS and WO_3 calculated with a log normal distribution function for CdS, W3, W5, W10 and W100

Figure 5 shows results of EDX analysis for comparison between (a) pure WO_3 and (b) WO_3 -CdS composite. Figure 5 (c), (d), (e) and (f) shows the mapping of W5 for each element of Cd, S, W and O. The EDX analysis conducted on the WO_3 -CdS composite reveals a compelling insight into the distribution of elements within the material. The results showcase a remarkably even distribution of all constituent elements throughout the composite structure. This uniform distribution pattern strongly implies the effectiveness of the precipitation method employed in CdS onto the surface of WO_3 . The meticulous blending and interaction between WO_3 and CdS during the synthesis process have led to this homogeneous dispersion.

The close proximity and interaction between WO_3 and CdS, as illustrated in Figure 5 (b), are especially remarkable. This proximity suggests a high degree of interfacial contact between the two materials, setting the stage for intriguing possibilities. One of these possibilities is the potential for electron transfer to occur between WO_3 and CdS during photoexcitation events, a phenomenon that aligns with the well-established concept of Z-scheme electron transfer [25]. Where it involves the sequential transfer of electrons from one material to another, typically from a material with a lower energy level to a material with a higher energy level.

In this case, the observed close interaction between WO_3 , which is known to have suitable energy levels for water oxidation, and CdS, which can facilitate the reduction of water, suggests a conducive environment for efficient electron transfer during photocatalytic reactions. This structure provides an extended separation between charges that will increase the duration for electron-hole recombination. As a result, the photocatalyst will possess this generates a substantial growth in the photocatalytic activity of the photocatalysts [26]. The EDX analysis not only confirms the even distribution of elements within the WO_3 -CdS composite but also hints at the exciting potential for electron transfer processes between WO_3 and CdS, supporting the concept of Z-scheme electron transfer, which can significantly impact the photocatalytic capabilities of this composite material.

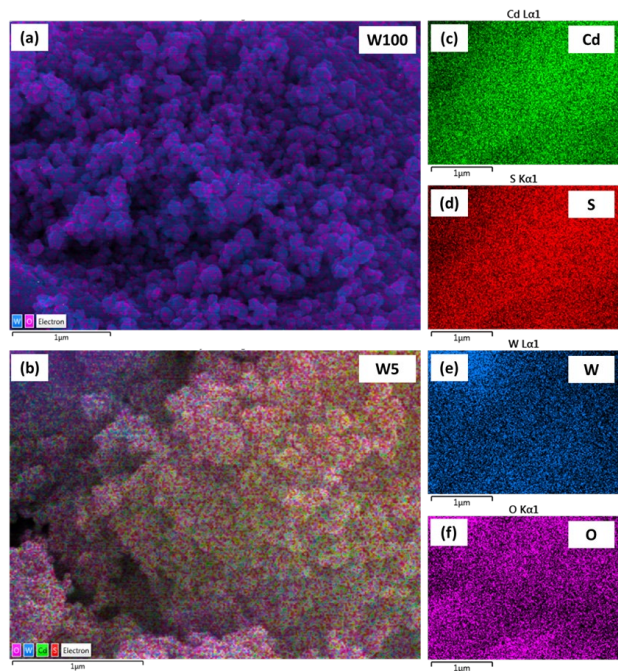


Figure 5 (a) EDX mapping of W100, and (b) W5 samples. (c) EDX mapping for W5 of Cd, (d) EDX mapping for W5 of S, (e) EDX mapping for W5 of W, (f) EDX mapping for W5 of O

Figure 6 presents the EDX analyses of two key samples: (a) W5 and (b) W100, each representing different weight percentages of the composite's constituent elements. The peaks were labelled with corresponding elements. For those unlabelled peaks, these peaks arisen due to impurities of the sample, which originated from the carbon tapes or coating involved during the EDX analysis [27]. Nevertheless, for the purpose of this comparison, considering EDX sample preparation as the source, these impurities have been disregarded and only the primary elements of interest have been considered.

A comprehensive summary of the atomic percentages, derived from the EDX analysis, is thoughtfully presented in Table 2. This meticulous comparison involves assessing the atomic percentages against the initially calculated theoretical stoichiometry weight percentages. The close correspondence observed between the WO_3 and CdS and their respective theoretical values is particularly noteworthy.

The findings from both FESEM and EDX analyses provide strong evidence about how the WO_3 -CdS composite photocatalyst is structured. It becomes clear that when it's made, the WO_3 particles act as a sturdy base that supports the smaller CdS particles. This complex arrangement is visually portrayed in Figure 7, where it becomes evident that the smaller CdS particles form on the surfaces of the larger WO_3 particles [28]. This structural configuration holds significant promise for enhancing the photocatalytic efficiency of the composite. It enables close interparticle interactions and facilitates efficient charge transfer processes between the materials.

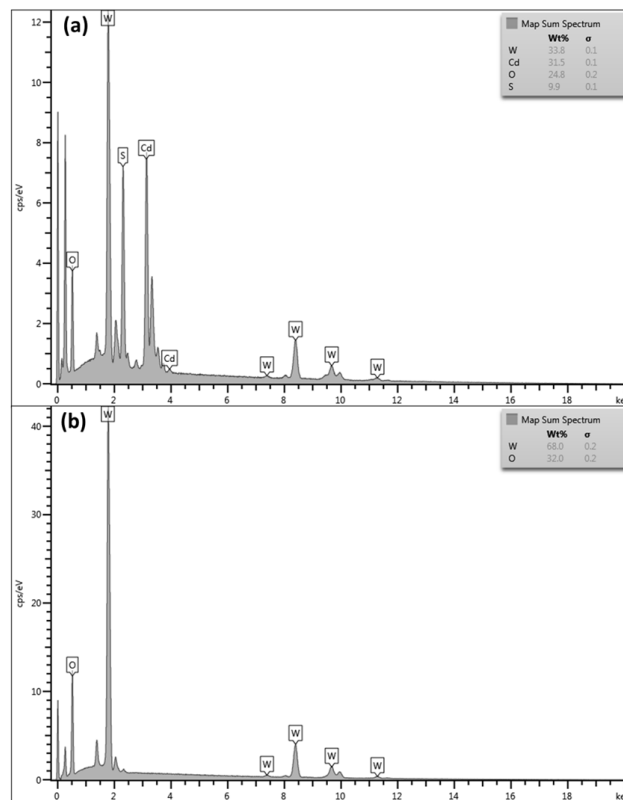


Figure 6 EDX analysis of (a) W5 and (b) W100 sample. Inset diagram shows the weight percentages of each elements.

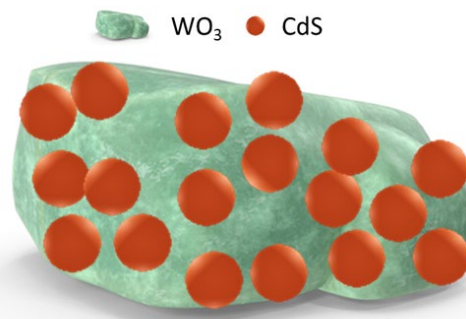


Figure 7 Illustration on formation of WO_3 -CdS photocatalyst

3.2 Chemical Structure Analysis of (WO_3 -CdS) Composite Photocatalysts

Analysis of the FTIR spectrograph, as shown in Figure 8 (a), offers valuable insights into the molecular vibrations and chemical bonds present in the examined materials, namely CdS, WO_3 , and the WO_3 -CdS composites. When examining the FTIR spectrum of CdS, several notable features come into focus. First and foremost, a broad absorption peak spanning from 525 cm^{-1} to 880 cm^{-1} is observed. This broad peak indicates the presence of multiple vibrational modes involving chemical bonds within the CdS material. Additionally, a distinctive and sharp absorption peak appears at 1038 cm^{-1} . This particular peak is assigned to a specific type of molecular vibration known as the Cd-S stretching mode [29, 30].

The Cd-S stretching mode is a characteristic vibrational pattern that arises due to the interactions between cadmium and sulfur atoms within the CdS compound. It signifies the stretching and contraction of the chemical bonds between these atoms. The presence of this peak in the FTIR spectrum provides clear evidence of the Cd-S bonds within the CdS material.

For the W3, W5 and W100, weaker band appears at 1008 cm^{-1} that is associated with stretching of W=O bond, indicating the presence of double bonds between tungsten and oxygen atoms on the surface of the composite materials [31]. Further analysis reveals distinct peaks at 1386 cm^{-1} and 1624 cm^{-1} which can be assigned to stretching and bending vibration of W-O bonds [32].

For the WO_3 -CdS composites, specifically W3 and W5, several distinct absorption features become evident. One of the most prominent absorptions occurs at 835 cm^{-1} . This peak relates to the stretching vibration modes of O-W-O bonds within the composite structure [33].

Figure 8 (b) shows FTIR transmittance peak located at 3434 cm^{-1} region that can be relate to the stretching modes of O-H groups in water or hydroxyl (OH) groups [34]. These features suggest the existence of water or hydroxyl groups on the surface or within the composite material. A much broader and almost imperceptible peak at for CdS indicates greater extent of water absorption.

Upon thorough examination of the consistent pattern observed in the samples labelled as W3 and W5, it becomes apparent that they exhibit similar spectral characteristics. These similarities imply that a comparable spectrum for the W10 sample. Consequently, there was a decision to omit presenting the results for the W10 sample, as it was expected to follow the same trend as W3 and W5.

One of the significant pattern that can be observed, is the evolution of the peaks matching to WO_3 as the weight percentages of WO_3 in the composite increase. This evolution is strikingly evident in the W100 sample, where these peaks become more well-defined and pronounced. Essentially, as the concentration of WO_3 increases, the spectral signals associated with WO_3 become sharper and clearer. This phenomenon is a valuable indicator of the increasing dominance of WO_3 within the composite.

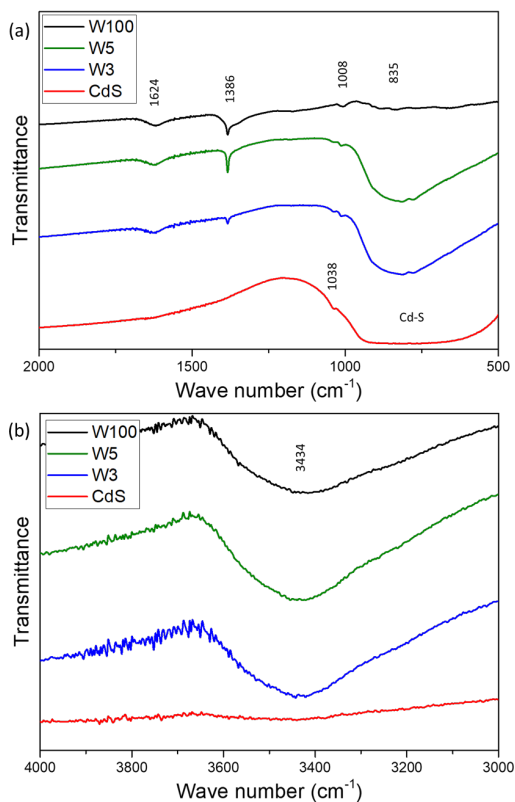


Figure 8 FTIR spectrums of CdS, W3, W5 and W100

3.3 Physical Structure Analysis of (WO_3 -CdS) Composite Photocatalysts

To gain insights into structural characteristics, of WO_3 , synthesized CdS, and WO_3 -CdS composites, their crystal structure and purity was examined. The results were analysed using XRD, and the patterns obtained are illustrated in Figure 9.

In the case of CdS, the XRD pattern exhibited distinct and well-defined reflection peaks corresponding to specific crystallographic planes, namely (002), (110), and (112). These peaks were observed at angles of 26.53° , 43.81° , and 51.89° , respectively. These angles are indicative of the hexagonal structure of CdS. The presence of such well-defined peaks suggests the high crystallinity of the CdS material.

Conversely, when examining the WO_3 -CdS composites, labelled as W3 and W5, a different pattern emerged. These composites displayed a combination of peaks attributed to both CdS and WO_3 . Importantly, these peaks were notably strong and sharp, indicative of high-quality diffraction patterns. The presence of WO_3 peaks was particularly striking, appearing at various angles, including 22.9° , 23.4° , 24.1° , 26.4° , 32.8° , 33.1° , 33.9° , 41.6° , 49.82° , and 50.43° . These angles corresponded to different crystallographic planes, such as (002), (020), (200), (120), (022), (202), (220), (222), (232), and (114), consistent with the monoclinic configuration of WO_3 .

The presence of these well-defined peaks in the XRD spectra strongly signifies the successful synthesis of the WO_3 -CdS composites using the precipitation method. It is worth noting that similar XRD patterns were expected for W10, and therefore, those specific results have not been included here.

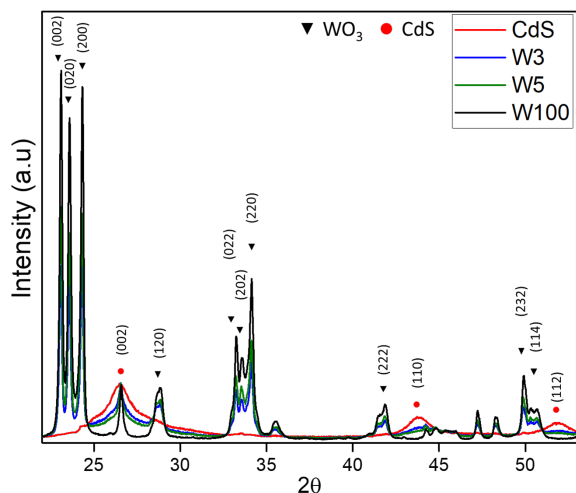


Figure 9 XRD analysis for CdS, W3, W5 and W100 photocatalysts

3.4 Optical Structure Analysis of (WO₃-CdS) Composite Photocatalysts

In this study, the transmittance spectrogram of the photocatalysts are illustrated in Figure 10, and the apparent band gap of the photocatalyst powders was determined. This determination was achieved using a method known as the Kubelka-Munk approximation, which involves constructing Tauc plots of $\alpha h\nu^{1/2}$ against $h\nu$.

The attained apparent band gap values are compiled in Table 2, and for reference, the values of pure CdS and WO₃, labelled as W100, from previous studies are also included. Values for CdS is 2.4 eV while value for W100 range from 2.5 eV to 2.8 eV [34, 35, 36]. One of significant discovery is that the composites of WO₃-CdS exhibit lower band gap energy values compared to both pure CdS and pure WO₃. Specifically, the W3 and W5 composites have achieved band gap energies of approximately 2.285 eV and 2.287 eV, respectively, whereas the W10 composite displays a slightly lower band gap energy of 2.238 eV.

This decrease in band gap energy observed in the W3 and W5 composite is attributed to the increases in the size of the CdS particles within the composite. Band gap energy of a semiconductor like CdS is generally determined by its size, with smaller particles having a larger band gap and larger particles having a smaller band gap. This behavior is a consequence of quantum confinement effects in nanomaterials where confinement of charge carriers (electrons and holes) within the small size of the particle results in discrete energy levels [38]. Essentially, larger CdS particles have a lower band gap energy because they experience reduced quantum confinement effects compared to smaller nanoparticles.

However, it's noteworthy that despite CdS particle size is considerably smaller for W10 compared to CdS particles in W3 and W5, the band gap energy value is even lower. This intriguing observation may be attributed to the synergistic effects that arise when WO₃ is incorporated into the composite.

WO₃ is esteemed for its remarkable proficiency in efficiently segregating charge carriers, primarily attributed to three pivotal characteristics. Firstly, WO₃ showcases a notable electron mobility, facilitating the effortless traversal of electrons through the material. This heightened mobility

expedites the rapid dispersion of electrons from their origination points, thus diminishing the probability of recombination with holes.

Moreover, WO₃ boasts the capacity to adeptly capture and immobilize holes, thwarting their migration and subsequent recombination with electrons. These confined holes tend to localize within specific sectors of the material, establishing a concentration gradient that further propels electron migration away from these localized zones.

Furthermore, the energy band structure of WO₃ forges a potential barrier, effectively serving as a partition separating electrons from holes. This barrier hinders the recombination process, as electrons require a specific level of energy to surmount it and combine with holes. This efficient charge separation mechanism contributes to a reduced effective band gap for initiating photocatalytic reactions, ultimately improving the composite photocatalytic activity.

This observation is significant because it supports the concept of a Z-scheme electron transfer mechanism. In this mechanism, the reduction in the band gap energy acts akin to a linchpin in prolonging the recombination time between electrons and holes, which are produced during photocatalytic reactions. By minimizing the recombination of these charge carriers, the photocatalyst overall performance is significantly enhanced, making it more efficient at harnessing light energy for chemical reactions.

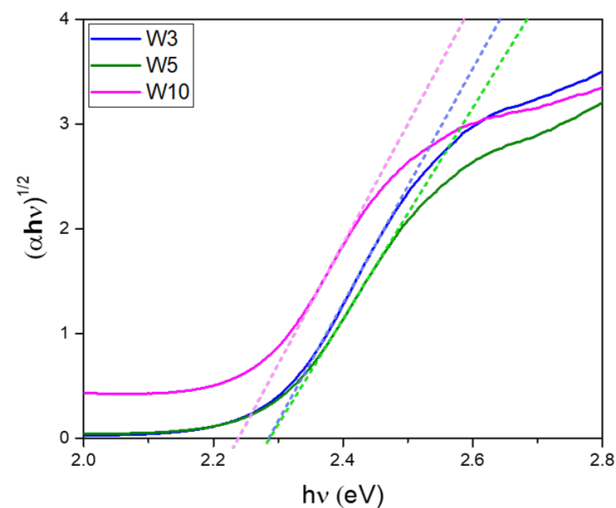


Figure 10 UV-vis spectra of $\alpha h\nu^{1/2}$ against $h\nu$

Table 2 Band gap of CdS, WO₃-CdS and WO₃ photocatalysts

Photocatalyst	Band Gap Energy (eV)
CdS	2.4* [35]
W3	2.285
W5	2.287
W10	2.238
W100	2.5 – 2.8* [36]

3.5 Performance of (WO₃-CdS) Composite Photocatalysts

To examine the photocatalytic potential of the synthesized WO₃-CdS catalysts, photocatalytic degradation of reactive orange 16 (RO16) solution has been performed under visible light irradiation. To ensure that adsorption did not occur during the photocatalytic degradation and potentially affect its

performance, we evaluated the adsorption capacity of the prepared $\text{WO}_3\text{-CdS}$ catalysts through a prior photocatalyst adsorption test of RO16 in an aqueous solution.

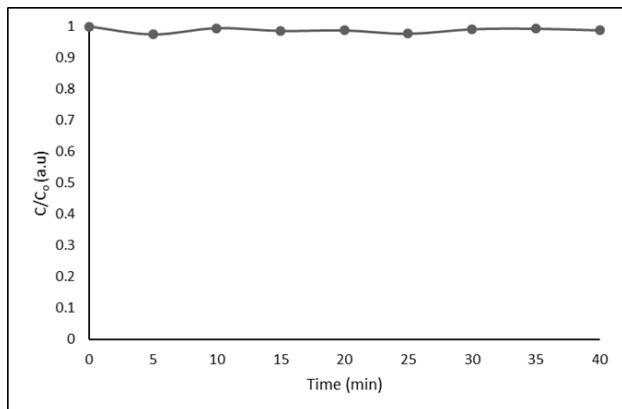


Figure 11 The adsorption of normalize C/C_0 of RO16 concentration with respect to time without irradiation of light for $\text{WO}_3\text{-CdS}$ catalyst

Figure 11 illustrates the adsorption activity of RO16 on $\text{WO}_3\text{-CdS}$ without visible light irradiation, a process that was carried out for 40 minutes. The graph reveals that initially, in the first 25 minutes, there are adsorption and desorption effects, as indicated by slight variations in the C/C_0 ratio. However, after 30 minutes, the adsorption capacity of the prepared $\text{WO}_3\text{-CdS}$ reached equilibrium, as there were no significant decreases observed beyond this point. Besides that, other studies have reported that 30 minutes to be long enough for adsorption of the WO_3 and CdS photocatalysts to attain equilibrium [38, 39, 40].

The observed lack of significant adsorption when there is no illumination, as reported in former studies and akin to the behaviour noted for WO_3 photocatalysts [42], where photocatalysts, like WO_3 , typically do not exhibit strong adsorption capabilities in the dark. Adsorption and subsequent photocatalytic reactions are initiated when the photocatalyst absorbs photons and generates electron-hole pairs.

Additionally, there are other conceivable factors that must be taken into account. One possible explanation for this phenomenon could be attributed to suboptimal experimental conditions. The equilibrium adsorption capacity of photocatalysts can be influenced by various factors, including temperature, solution pH, initial dye concentration, and the quantity of photocatalyst employed [42, 43].

Low adsorption levels may occur when the experimental conditions are not precisely tailored to the specific adsorbent-adsorbate system under investigation. For instance, the temperature may not be within the optimal range, potentially being either too high or too low. Likewise, the initial concentration of the adsorbate may not reach a level that ensures efficient adsorption. Consequently, in this experimental setup, each sample was subjected to visible light irradiation after a 30-minute period to standardize the experiment.

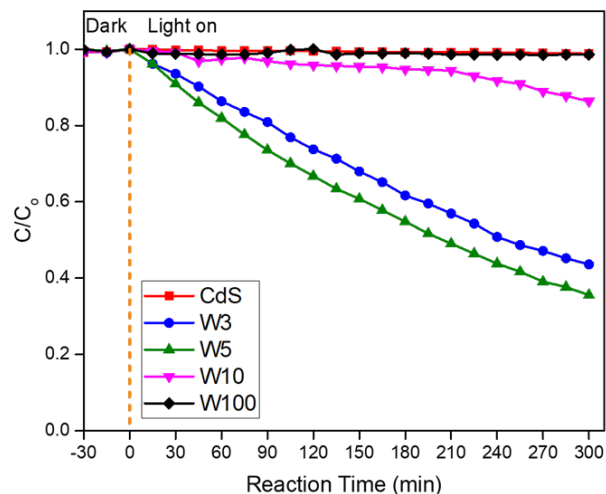


Figure 12 The ratio of normalize degradation (C/C_0) of RO16 concentration

To analyze the performance of CdS, W3, W5, W10 and W100, the photocatalysts were tested against degradation of RO16 when illuminated with visible light. After the catalysts and RO16 solution underwent adsorption for 30 minutes, reaching equilibrium, the visible light source was activated, and readings were recorded continuously for a duration of up to 300 minutes. Figure 12 shows both pure CdS and W100 does not show any significant degradation of RO16 which is less than 1.18 % of degradation. The findings for CdS are consistent with another study, indicating that CdS is susceptible to light-induced corrosion when exposed to water-based surroundings on its own [10]. On the other hand, W100 exhibits ineffective photocatalyst performance due to rapid photoelectron and hole recombination, a finding similar to that reported in another study [45]. This characteristic renders both CdS and WO_3 unsuitable for use as photocatalysts on their own.

Moreover, Figure 11 shows that the best degradation rate can be up to 64.45 % in 300 minutes for W5 photocatalyst. In contrast, higher weight percentages of WO_3 (W10) showed less photocatalytic activities due to couple of possibilities. One potential explanation for the observed phenomenon can be attributed to the presence of an excessive amount of WO_3 content within the photocatalytic system. This surplus WO_3 may inadvertently coat or obscure the active sites on the surface of CdS particles. When these active sites become obstructed by excess WO_3 , it can hinder the accessibility of photons to the CdS particles. Consequently, this reduction in the availability of active sites for photon absorption can hamper the performance of charge separation, a critical stage in the photocatalytic process. Another possibility to consider is a reduction in the sizes of the CdS particles in the system. In photocatalysis, smaller particles generally exhibit superior photocatalytic properties owing to their greater surface area relative to volume, providing more active sites for reactions. However, if the CdS particles have diminished in size beyond an optimal range, it can significantly compromise their photocatalytic efficiency. Smaller particles may have fewer available active sites for photon absorption and electron-hole pair generation, instigating the observed decline in overall photocatalytic activity.

Furthermore, the degradation of RO16 from $\text{WO}_3\text{-CdS}$ photocatalyst under visible light irradiation is matched to

pseudo first order kinetics equation, $\ln(C/C_0) = kt$ where k is the rate constant and t is irradiation time. A linear relationship between $\ln(C/C_0)$ and t is shown in Figure 13 where it illustrates that among WO_3 -CdS photocatalysts composite, W5 exhibits the highest photocatalytic performance with highest rate constant k value of 0.0034. This conclude that W5 to be the best combination of WO_3 -CdS composite due to high recombination time following the proposed Z-scheme photocatalytic mechanism.

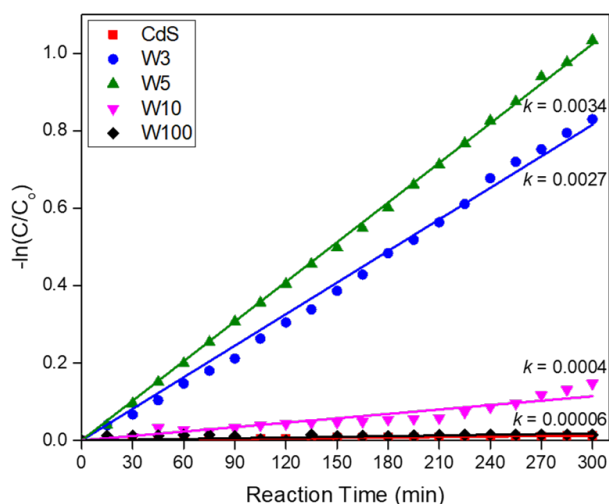


Figure 13 The normalized $-\ln C/C_0$ of RO16 concentration against visible light irradiation time for WO_3 -CdS

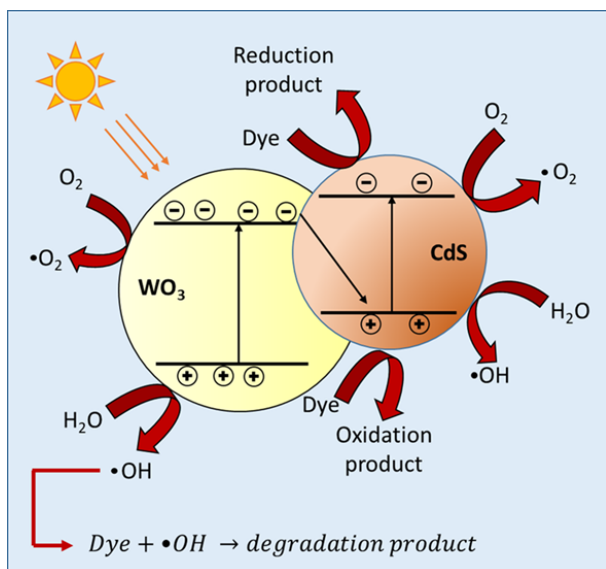


Figure 14 Diagrammatic representation of the Z-scheme formation in WO_3 -CdS composites, tailored to promote electron transfer and lengthen the time before electrons and holes recombine

The remarkable improvement in photocatalytic activity detected in all the WO_3 -CdS photocatalysts in comparison to pure WO_3 and CdS might be credited to the proposed Z-scheme electron transfer mechanism. This mechanism performs a vital task in enhancing the overall performance of the composite photocatalyst. As depicted in Figure 14, the schematic diagram illustrates the configuration of a Z-scheme that facilitates

proficient electron transfer from WO_3 to CdS, effectively extending the recombination time of electrons and holes.

The creation of the Z-scheme diagram is formed on the band energy alignment of the two composite photocatalysts. It is essential for the valence energy of one photocatalyst (CdS) to occupy the energy level between the valence and conduction bands of the other photocatalyst (WO_3) [46]. In this particular proposed Z-scheme electron transfer process, the strategic arrangement of the two photocatalysts, WO_3 and CdS, plays a crucial role. More specifically, it directs its attention towards the conduct of stimulated electrons situated within the lower conduction band of WO_3 .

When electrons, nestled within a substance, assimilate energy from incoming photons, a profound metamorphosis unfolds within their energy state. Ordinarily, these electrons inhabit what is termed the valence band, symbolizing the material's steadfast and low-energy arrangement. Nevertheless, upon absorbing energy from photons, frequently as a consequence of exposure to light, they experience a marked and consequential alteration. This infusion of energy propels them into a higher energy level termed the conduction band.

This transition from the valence band to the conduction band, driven by the absorption of energy, is often described as the electrons becoming "excited." In their excited state, these electrons carry an excess of energy. However, in the absence of any mechanisms to facilitate their movement, these excited electrons can lose their kinetic energy over time and return to the valence band, a process known as recombination.

Within the scope of this Z-scheme, what is significant is that these excited electrons are directed to transfer to CdS instead of recombining with holes within their own photocatalyst (WO_3). This redirection of electrons is enabled by the band energy alignment discussed earlier. CdS, with its specific band structure, provides a favourable energetic pathway for these electrons to move toward it, preventing their recombination with holes in WO_3 .

In light of this directed electron transferral, the existence of electron vacancies (holes) within the valence band of WO_3 is prolonged. These holes are highly reactive and have the potential to engage in oxidation reactions with pollutant molecules present in the surrounding environment. This extended existence of holes in the valence band boost the potential of these oxidation reactions occurring, ultimately leading to the degradation of pollutants.

In essence, the Z-scheme mechanism ensures that the excited electrons, which carry the potential for driving reduction reactions, are efficiently transferred to CdS, allowing WO_3 to maintain a pool of reactive holes. This concerted action enhances the photocatalytic activity of the composite, making it highly effective in degrading pollutants through both oxidation and reduction processes.

Moreover, both photocatalysts in this composite are responsive to visible light, further enhancing the Z-scheme's effectiveness. The higher conduction band energy of CdS allows it to absorb visible light energy and excite its own electrons [47]. As these holes are filled by electrons from WO_3 , CdS electrons linger in the conduction band, increasing the probability of reduction reactions with pollutants. This Z-scheme formation significantly extends the recombination time of charge carriers, ensuing in a marked enhancement in the photocatalytic degradation performance [17].

To provide a clear overview of these findings, a comparison table (Table 3) was created to compare the outcomes of this study with those of other pertinent literature sources. This table serves as a valuable reference to showcase the superior photocatalytic activity achieved through the Z-scheme electron transfer mechanism in WO₃-CdS composite photocatalysts.

Table 3 Comparison of present work with other recent literatures

Sample	Dye used	Degradation efficiency (%)	Reaction time (min)	References
Ag WO ₃	Acid Red 88	~29	120	[48]
Ag/CuO/WO ₃	Acid Red 88	~62	120	[48]
WO ₃ /g-C ₃ N ₄	Rhodamine B	62	90	[49]
CdS/TiO ₂	Rhodamine B	60	120	[50]
CdS/LaFeO ₃	Methylene blue	46	180	[51]
CdS	RO16	1.18	300	This study
WO ₃	RO16	1.48	300	This study
WO ₃ -CdS	RO16	64.45	300	This study

4.0 CONCLUSION

Pure CdS and WO₃-CdS composite were prepared as photocatalysts using precipitation method for photocatalytic degradation of RO16. FESEM inspections revealed the uniform distribution of WO₃ and CdS while FTIR, XRD analysis supported the formation WO₃-CdS composite. Band gap energy analysis shows that WO₃-CdS composite have lower band gap energy compared to pure W100 which is 2.28 eV. The research findings indicate that the WO₃-CdS composite demonstrates notably superior photocatalytic performance in comparison to both pure CdS and W100. When exposed to visible light, the most efficient blend was determined to be W5, which accomplished a degradation rate of 64.45 % within a 300-minute timeframe, with a degradation reaction rate constant (*k*) value of 0.0034.

The results obtained in this study serve to emphasize and reinforce the significance of the proposed Z-scheme electron transfer mechanism. This mechanism is a fundamental aspect of the composite photocatalyst operation, and it Assumes a pivotal role in markedly enhancing its photocatalytic efficacy.

To elaborate further, the Z-scheme electron transfer mechanism is a sophisticated process that ensures the effectual utilization of photons in the photocatalytic system. When visible light irradiates the WO₃-CdS composite photocatalyst, the Z-scheme helps the seamless transfer of excited electrons from one photocatalyst component to another. This process will significantly extend the lifespan of these charge carriers, by preventing their premature recombination. As consequences, the composite photocatalyst able maximizes its capability to initiate chemical reactions, which are vital for the degradation of pollutants.

While it has been established that, dye wastewater habitually contains complex and persistent organic pollutants that can be difficult to be remove through conventional treatment methods, WO₃-CdS composite photocatalyst transpires to be an ideal candidate for addressing this environmental challenges, due to its remarkable effectiveness to harness visible light for photocatalytic activity.

The potential of this composite photocatalyst is not only limited to laboratory setting, in fact, it holds potential for practical industrial applications such as integrating the photocatalyst into a dual-layer hollow fiber membrane system. The dual-layer hollow fiber membrane, combined with the photocatalytic properties of the composite and its reusability, can efficiently remove contaminants from water sources for water purification and wastewater treatment. This will provide an interesting alternative solution to industries concerned with environmental protection and enhancement.

Additionally, the versatility of WO₃-CdS photocatalyst opens the door to further advancements. Example of its versatility is that this photocatalyst functionality can be extended through additional precipitation methods to incorporate with compatible materials. This expansion enables the formation of novel double Z-scheme electron transfer systems where these systems have the potential to revolutionize energy storage photocatalysts, enabling the efficient conversion and storage of energy from light sources. This innovation holds considerable significance for the development of sustainable and clean energy solutions, as it harnesses the power of photocatalysis to contribute to energy generation and storage technologies.

In summary, the composite photocatalyst showcased in this study not only has immediate applications in industrial processes like membrane technology but also presents exciting opportunities for advancing energy storage technologies. Its adaptability and performance make it a versatile tool with the potential to address critical challenges in both environmental and energy-related fields, aligning with the growing emphasis on sustainability and clean energy solutions.

Acknowledgement

The authors gratefully acknowledge the financial support from Universiti Teknologi Malaysia under Fundamental Research (Project Number: Q.J130000.3809.22H07), UTM High Impact Research (Project Number: Q.J130000.2409.08G34), Matching Grant (Project Number: Q.J130000.3009.03M15). In addition, the authors also would like to acknowledge the financial support from UMW for the Research Contract grant (Project Number: R.J130000.7609.4C471 and R.J130000.7609.4C497).

Conflicts of Interest

The author(s) declare(s) that there is no conflict of interest regarding the publication of this paper

References

- [1] M. J. Plater, A. Raab, and H. Hartmann. 2020. "Liquid chromatography–mass spectrometry analysis of cationic aniline dyes from the Technical University of Dresden Historical Collection of Dyes," *Journal of Chemical Research*, 44(5–6): 326–335.
- [2] H. Zollinger. 2003. *Color Chemistry: Syntheses, Properties, and Applications of Organic Dyes and Pigments*. John Wiley & Sons.
- [3] A. D. Broadbent. 2003. "Basic principles of textile coloration," *Color Research & Application*, 28(3): 230–231. DOI: 10.1002/col.10152.
- [4] U. Sirimahachai, H. Harome, S. Wongnawa, and others. 2017. "Facile synthesis of AgCl/BiVO₃ composite for efficient photodegradation of RO16 under UV and visible light irradiation," *Sains Malaysiana*, 46(9):

- 1393–1399.
- [5] Y. Zhou, J. Lu, Y. Zhou, and Y. Liu. 2019. "Recent advances for dyes removal using novel adsorbents: A review," *Environmental Pollution*, 252: 352–365. DOI: 10.1016/j.envpol.2019.05.072.
- [6] A. Khatri, M. H. Peerzada, M. Mohsin, and M. White. 2015. "A review on developments in dyeing cotton fabrics with reactive dyes for reducing effluent pollution," *Journal of Cleaner Production*, 87(1): 50–57. DOI: 10.1016/j.jclepro.2014.09.017.
- [7] M. M. Khan, S. F. Adil, and A. Al-Mayouf. 2015. "Metal oxides as photocatalysts," *Journal of Saudi Chemical Society*, 19(5): 462–464. DOI: 10.1016/j.jsccs.2015.04.003.
- [8] S. G. Kumar and L. G. Devi. 2011. "Review on modified TiO₂ photocatalysis under UV/visible light: Selected results and related mechanisms on interfacial charge carrier transfer dynamics," *Journal of Physical Chemistry A*, 115(46): 13211–13241. DOI: 10.1021/jp204364a.
- [9] B. P. Sampson, A. M. Secrest, C. B. Hansen, and A. C. Geller. 2018. "Examining Dermatologist Use and Opinions of Ultraviolet Radiation for Cosmetic and Medical Purposes," *The Journal of Clinical and Aesthetic Dermatology*, 11(2): 41–46.
- [10] M. Pelaez et al. 2012. "A review on the visible light active titanium dioxide photocatalysts for environmental applications," *Applied Catalysis B: Environmental*, 125: 331–349. DOI: 10.1016/j.apcatb.2012.05.036.
- [11] S. Wang, B. Zhu, M. Liu, L. Zhang, J. Yu, and M. Zhou. 2019. "Direct Z-scheme ZnO/CdS hierarchical photocatalyst for enhanced photocatalytic H₂-production activity," *Applied Catalysis B: Environmental*, 243: 19–26.
- [12] S. Shenoy, E. Jang, T. J. Park, C. S. Gopinath, and K. Sridharan. 2019. "Cadmium sulfide nanostructures: Influence of morphology on the photocatalytic degradation of erioglaucine and hydrogen generation," *Applied Surface Science*, 483(April): 696–705. DOI: 10.1016/j.apsusc.2019.04.018.
- [13] M. B. Tahir, S. Ali, and M. Rizwan. 2019. "A review on remediation of harmful dyes through visible light-driven WO₃ photocatalytic nanomaterials," *International Journal of Environmental Science and Technology*, 16(8): 4975–4988. DOI: 10.1007/s13762-019-02385-5.
- [14] Q. Zhang, Y. Liu, Z. Xu, Y. Zhao, M. Chaker, and D. Ma. 2017. "Visible-light-driven photocatalysis," *Nanomaterials for Energy Conversion and Storage*, p. 109.
- [15] F. Zhou, C. Yan, Q. Sun, and S. Komarneni. 2019. "TiO₂/Sepiolite nanocomposites doped with rare earth ions: Preparation, characterization and visible light photocatalytic activity," *Microporous and Mesoporous Materials*, 274: 25–32. DOI: 10.1016/j.micromeso.2018.07.031.
- [16] M. Hu et al. 2020. "NiS/BiOBr hybrids with retarded carrier recombination and enhanced visible-light-driven photocatalytic activity," *Journal of Materials Science*, 55(10): 4265–4278. DOI: 10.1007/s10853-019-04288-9.
- [17] T. Di, Q. Xu, W. K. Ho, H. Tang, Q. Xiang, and J. Yu. 2019. "Review on Metal Sulphide-based Z-scheme Photocatalysts," *ChemCatChem*, 11(5): 1394–1411. DOI: 10.1002/cctc.201802024.
- [18] C. Song, X. Wang, J. Zhang, X. Chen, and C. Li. 2017. "Enhanced performance of direct Z-scheme CuS-WO₃ system towards photocatalytic decomposition of organic pollutants under visible light," *Applied Surface Science*, 425: 788–795.
- [19] A. Meng, B. Zhu, B. Zhong, L. Zhang, and B. Cheng. 2017. "Direct Z-scheme TiO₂/CdS hierarchical photocatalyst for enhanced photocatalytic H₂-production activity," *Applied Surface Science*, 422: 518–527.
- [20] J. Jin, J. Yu, D. Guo, C. Cui, and W. Ho. 2015. "A Hierarchical Z-Scheme CdS-WO₃ Photocatalyst with Enhanced CO₂ Reduction Activity," *Small*, 11(39): 5262–5271. DOI: 10.1002/sml.201500926.
- [21] S. K. Paswan et al. 2021. "Optimization of structure-property relationships in nickel ferrite nanoparticles annealed at different temperature," *Journal of Physics and Chemistry of Solids*, 151: 109928.
- [22] B. Sinha, R. H. Müller, and J. P. Möschwitzer. 2013. "Bottom-up approaches for preparing drug nanocrystals: Formulations and factors affecting particle size," *International Journal of Pharmaceutics*, 453(1): 126–141. DOI: 10.1016/j.ijpharm.2013.01.019.
- [23] M. Schmitt. 2015. "Synthesis and testing of ZnO nanoparticles for photo-initiation: Experimental observation of two different non-migration initiators for bulk polymerization," *Nanoscale*, 7: April. DOI: 10.1039/C5NR00850F.
- [24] S. Salatin, J. Barar, M. Barzegar-Jalali, K. Adibkia, F. Kiafar, and M. Jelvehgari. 2017. "Development of a nanoprecipitation method for the entrapment of a very water-soluble drug into Eudragit RL nanoparticles," *Research in Pharmaceutical Sciences*, 12(1): 1–14. DOI: 10.4103/1735-5362.199041.
- [25] L. Ye, J. Liu, C. Gong, L. Tian, T. Peng, and L. Zan. 2012. "Two different roles of metallic Ag on Ag/AgX/BiOX (X = Cl, Br) visible light photocatalysts: Surface plasmon resonance and Z-Scheme bridge," *ACS Catalysis*, 2(8): 1677–1683. DOI: 10.1021/cs300213m.
- [26] M. Ou et al. 2018. "Hierarchical Z-scheme photocatalyst of g-C₃N₄@Ag/BiVO₄ (040) with enhanced visible-light-induced photocatalytic oxidation performance," *Applied Catalysis B: Environmental*, 221(September): 97–107. DOI: 10.1016/j.apcatb.2017.09.005.
- [27] E. Klugmann-Radziemska and M. Rudnicka. 2020. "Decrease in Photovoltaic Module Efficiency because of the Deposition of Pollutants," *IEEE Journal of Photovoltaics*, 10(6): 1772–1779. DOI: 10.1109/JPHOTOV.2020.3013971.
- [28] J. Mao et al. 2019. "Insights into photocatalytic inactivation mechanism of the hypertoxic site in aflatoxin B₁ over clew-like WO₃ decorated with CdS nanoparticles," *Applied Catalysis B: Environmental*, 248: 477–486.
- [29] G. Roshini, V. Sathish, S. Manigandan, A. Tamilarasi, and E. Priyanka. 2022. "Synthesis, characterization of Ag-doped CdS-WO₂ nanocomposite and effects of photocatalytic degradation in RhB under visible light irradiation."
- [30] N. Pourshirband, A. Nezamzadeh-Ejhieh, and S. N. Mirsattari. 2021. "The CdS/g-C₃N₄ nano-photocatalyst: Brief characterization and kinetic study of photodegradation and mineralization of methyl orange," *Spectrochimica Acta Part A: Molecular and Biomolecular Spectroscopy*. 248: 119110. DOI: https://DOI.org/10.1016/j.saa.2020.119110.
- [31] A. Cremonesi, D. Bersani, P. P. Lottici, Y. Djaoed, and P. V. Ashrit. 2004. "WO₃ thin films by sol-gel for electrochromic applications," *Journal of Non-Crystalline Solids*, 345–346: 500–504.
- [32] J. Sungpanich, T. Thongtem, and S. Thongtem. 2014. "Photocatalysis of WO₃ nanoplates synthesized by conventional-hydrothermal and microwave-hydrothermal methods and of commercial WO₃ nanorods," *Journal of Nanomaterials*, 2014: 131.
- [33] M. S. Belardja, H. Djelad, M. Lafjah, F. Chouli, and A. Benyoucef. 2020. "The influence of the addition of tungsten trioxide nanoparticle size on structure, thermal, and electroactivity properties of hybrid material-reinforced PANI," *Colloid and Polymer Science*, 298(11): 1455–1463.
- [34] W. L. Lachore, F. G. Hone, D. M. Andoshe, N. A. Tegegne, and M. A. Mekonnen. 2022. "Copper and nickel co-doping effects on the structural, optical and electrical properties of tungsten trioxide nanoparticles prepared by co-precipitation technique," *Materials Research Express*, 9(3): 35008.
- [35] S. A. Mirsalari and A. Nezamzadeh-Ejhieh. 2020. "Focus on the photocatalytic pathway of the CdS-AgBr nano-catalyst by using the scavenging agents," *Separation and Purification Technology*, 250: 117235.
- [36] N. A. Mohd Razali, W. N. Wan Salleh, F. Aziz, L. W. Jye, N. Yusof, and A. F. Ismail. 2021. "Review on tungsten trioxide as a photocatalyst for degradation of recalcitrant pollutants," *Journal of Cleaner Production*, 309: 127438. DOI: 10.1016/J.JCLEPRO.2021.127438.
- [37] T. Zhu, M. N. Chong, and E. S. Chan. 2014. "Nanostructured tungsten trioxide thin films synthesized for photoelectrocatalytic water oxidation: a review," *ChemSusChem*, 7(11): 2974–2997.
- [38] M. Sathish and R. P. Viswanath. 2007. "Photocatalytic generation of hydrogen over mesoporous CdS nanoparticle: Effect of particle size, noble metal and support," *Catalysis Today*, 129(3–4): 421–427.
- [39] R. C. Pawar, V. Khare, and C. S. Lee. 2014. "Hybrid photocatalysts using graphitic carbon nitride/cadmium sulfide/reduced graphene oxide (gC₃N₄/CdS/RGO) for superior photodegradation of organic pollutants under UV and visible light," *Dalton Transactions*, 43(33): 12514–12527.
- [40] S. Dursun, S. N. Koyuncu, İ. Cihan Kaya, G. G. Kaya, V. Kalem, and H. Akyildiz. 2020. "Production of CuO-WO₃ hybrids and their dye removal capacity/performance from wastewater by adsorption/photocatalysis," *Journal of Water Process Engineering*,

- 36: 101390.
- [41] P.-Y. Kuang et al. 2016. "Embedding Au quantum dots in rimous cadmium sulfide nanospheres for enhanced photocatalytic hydrogen evolution," *Small*, 12(48): 6735–6744.
- [42] R. A. Senthil et al. 2019. "A facile single-pot synthesis of WO₃/AgCl composite with enhanced photocatalytic and photoelectrochemical performance under visible-light irradiation," *Colloids and Surfaces A: Physicochemical and Engineering Aspects*, 567: 171–183.
- [43] N. Mosallanejad and A. Arami. 2012. "Kinetics and isotherm of sunset yellow dye adsorption on cadmium sulfide nanoparticle loaded on activated carbon."
- [44] M. S. S. Dorraji, H. R. Ashjari, M. H. Rasoulifard, and M. Rastgouy-Houjaghan. 2017. "Polyurethane foam-cadmium sulfide nanocomposite with open cell structure: Dye removal and antibacterial applications," *Korean Journal of Chemical Engineering*, 34: 547–554.
- [45] M. Zhou et al. 2021. "WO₃/Ag₂CO₃ mixed photocatalyst with enhanced photocatalytic activity for organic dye degradation," *ACS Omega*, 6(40): 26439–26453.
- [46] W. Zhao et al. 2019. "A novel Z-scheme Ag₃VO₄/BiVO₄ heterojunction photocatalyst: Study on the excellent photocatalytic performance and photocatalytic mechanism," *Applied Catalysis B: Environmental*. 245(December): 448-458.DOI: 10.1016/j.apcatb.2019.01.001.
- [47] B. Shao et al. 2019. "A novel double Z-scheme photocatalyst Ag₃PO₄/Bi₂S₃/Bi₂O₃ with enhanced visible-light photocatalytic performance for antibiotic degradation," *Chemical Engineering Journal*, 368: 730–745. DOI: 10.1016/j.cej.2019.03.013.
- [48] S. S. Mehta et al. 2021. "RGO/WO₃ hierarchical architectures for improved H₂S sensing and highly efficient solar-driving photodegradation of RhB dye," *Scientific Reports*, 11(1): 5023.
- [49] J. Singh, A. Arora, and S. Basu. 2019. "Synthesis of coral-like WO₃/g-C₃N₄ nanocomposites for the removal of hazardous dyes under visible light," *Journal of Alloys and Compounds*, 808: 151734.
- [50] E. M. Hashem et al. 2021. "Novel Z-Scheme/Type-II CdS@ZnO/g-C₃N₄ ternary nanocomposites for the durable photodegradation of organics: Kinetic and mechanistic insights," *Chemosphere*, 277: 128730. DOI: 10.1016/J.CHEMOSPHERE.2020.128730.
- [51] T. Senasu, T. Chankhanittha, K. Hemavibool, and S. Nanan. 2021. "Visible-light-responsive photocatalyst based on ZnO/CdS nanocomposite for photodegradation of reactive red azo dye and ofloxacin antibiotic," *Materials Science in Semiconductor Processing*, 123: 105558. DOI: 10.1016/J.MSSP.2020.10555